

α scattering cross sections on ^{12}C with microscopic coupled-channel calculation

Yoshiko Kanada-En'yo

Department of Physics, Kyoto University, Kyoto 606-8502, Japan

Kazuyuki Ogata

Research Center for Nuclear Physics (RCNP), Osaka University, Ibaraki 567-0047, Japan

Department of Physics, Osaka City University, Osaka 558-8585, Japan and

Nambu Yoichiro Institute of Theoretical and Experimental Physics (NITEP), Osaka City University, Osaka 558-8585, Japan

α elastic and inelastic scattering on ^{12}C is investigated with the coupled-channel calculation using microscopic α - ^{12}C potentials, which are derived by folding the Melbourne g -matrix NN interaction with the matter and transition densities of ^{12}C . These densities are obtained by a microscopic structure model of the antisymmetrized molecular dynamics combined with and without the 3α generator coordinate method. The calculation reproduces satisfactorily well the observed elastic and inelastic cross sections at incident energies of $E_\alpha = 130$ MeV, 172.5 MeV, 240 MeV, and 386 MeV with no adjustable parameter. Isoscalar monopole and dipole excitations to the 0_2^+ , 0_3^+ , and 1_1^- states in the α scattering are discussed.

I. INTRODUCTION

Cluster structure is one of the essential aspects of nuclear systems. A variety of well developed cluster structures have been discovered in excited states of stable light nuclei and also unstable nuclei. In the past two decades, new types of multi- α cluster states have been theoretically suggested in light $Z = N$ nuclei, and experimental searching for new cluster states has been intensively performed (see Refs. [1–4] and references therein).

In the study of the nuclear clustering, 3α cluster states in ^{12}C have been attracting a great interest for a long time [3–5]. 3α -cluster models suggested various cluster states near and above the 3α threshold energy [2, 6–22], such as the 0_2^+ state with a cluster gas feature of weakly interacting three α particles, and higher 0^+ and 2^+ states in the excitation energy $E_x \sim 10$ MeV region. Properties and band structure of those cluster states are one of the main issues to be clarified. In spite of the success of 3α -cluster models in describing many excited states with cluster structures, the cluster models fail to describe properties of low-lying states of ^{12}C such as the 2_1^+ excitation energy and β -decay transitions from ^{12}B because the α -cluster breaking is omitted in the models. Microscopic calculations of ^{12}C with the antisymmetrized molecular dynamics (AMD) [23–25] and Fermionic molecular dynamics [26, 27] beyond the 3α -cluster models have been applied to ^{12}C and shown that the α -cluster breaking plays an important role not only in the low-lying states but also in transitions and spectra of cluster states [28–31]. Furthermore, *ab initio* calculations are being developing for structure study of ^{12}C [33–35].

On the experimental side, the α inelastic scattering has been proved to be a powerful tool for study of cluster states, because cluster states can be strongly populated by that process. For instance, the 2_2^+ at 9.84 MeV of ^{12}C has been recently discovered with the multipole decomposition analysis (MDA) in the $^{12}\text{C}(\alpha, \alpha')$ reaction experiments [36, 37]. The α inelastic scattering has been

used also for study of isoscalar monopole and dipole excitations in a wide energy range. In the MDA analysis of the $^{12}\text{C}(\alpha, \alpha')$ reaction, the significant strengths have been observed in the low-energy region below the energy region of the giant resonances [38], and theoretically described by the decoupling of the low-lying cluster modes from the compressive collective vibration modes of the giant resonances [39, 40].

In order to extract structure information of the excited states, α elastic and inelastic cross sections have been analyzed with reaction models [36, 38, 41–46]. To describe these cross sections, many attempts of the coupled-channel (CC) calculations have been performed with the optical potentials obtained using microscopic 3α -cluster models of ^{12}C such as the resonating group method (RGM) [9] and the α condensation model [18]. However, many of them encountered the overshooting problem of the 0_2^+ cross sections, the so-called “missing monopole strength” [43]. To circumvent this problem, phenomenological manipulation of the optical potentials have been done, for instance, an introduction of state-dependent normalization factors for the imaginary part of the potentials and the use of density-independent effective NN interactions instead of the density-dependent ones.

Recently, the g -matrix folding model has been developed for study of hadron scattering reactions, and the Melbourne NN interaction [48] is found to successfully describe the nucleon-nucleus and α -nucleus scattering cross sections for various nuclei and in a wide range of incident energies. For the α scattering on ^{12}C , the microscopic CC calculation with the Melbourne g -matrix interaction has been performed by Minomo and Ogata using the RGM transition density and succeeded to reproduce the 0_2^+ cross sections as well as the elastic cross sections [47]. One of the advantages is that there is no adjustable parameter in the g -matrix folding model because the density- and energy-dependences of the real and imaginary parts of the effective NN interaction were determined fundamentally from the g -matrix theory. It turns

out that this approach of the g -matrix folding model can be a promising tool to investigate cluster states of general nuclei by means of the α scattering if reliable transition densities are provided by structure model calculations.

In this paper, we adopt the g -matrix folding model with the Melbourne NN interaction and calculate the cross sections of the α scattering to the $0_{1,2,3}^+$, $1_{1,2}^-$, $2_{1,2}^+$, 3_1^- , and $4_{1,2}^+$ states of ^{12}C . The α -nucleus CC potentials are derived by folding the matter and transition densities of ^{12}C obtained by a microscopic structure model of the AMD combined with and without the 3α -cluster generator coordinate method (GCM). The calculated elastic and inelastic cross sections are compared with the observed data at incident energies of $E_\alpha = 130$ MeV, 172.5 MeV, 240 MeV, and 386 MeV [36, 38, 46, 49, 50]. The transitions to the $0_{2,3}^+$ and 2_2^+ states and also the isoscalar (IS) dipole transitions to the $1_{1,2}^-$ state are focused. In the comparison of the present CC calculation with the DWBA calculation, we discuss the CC effect to the elastic and inelastic cross sections. The result obtained with the RGM density is also shown in comparison with the present result with the AMD density.

The paper is organized as follows. Sections II and III describe the formulations of the structure and reaction calculations, respectively. The structure properties of ^{12}C are shown in Sec. IV and the α scattering cross sections are discussed in Sec. V. Finally, a summary is given in Sec. VI. The matter and transition densities of ^{12}C are shown in appendix A, and definitions of the transition operators, strengths, and form factors are given in appendix B.

II. STRUCTURE CALCULATION OF ^{12}C WITH AMD+VAP WITH AND WITHOUT 3α -CLUSTER GCM

The ground and excited states of ^{12}C are calculated with the variation after projection (VAP) in the AMD framework, in which the variation is performed for the spin-parity projected AMD wave function as done in Refs. [28, 29]. In addition, we combine the AMD+VAP with the 3α -cluster GCM. The AMD+VAP and 3α -cluster wave functions adopted in the present calculation are the same as those used in Ref. [39]. For details of the calculation procedures and wave functions of ^{12}C , the reader is referred to those references.

In the AMD method, a basis wave function is given by a Slater determinant,

$$\Phi_{\text{AMD}}(\mathbf{Z}) = \frac{1}{\sqrt{A!}} \mathcal{A}\{\varphi_1, \varphi_2, \dots, \varphi_A\}, \quad (1)$$

where \mathcal{A} is the antisymmetrizer, and φ_i is the i th single-particle wave function written by a product of spatial,

spin, and isospin wave functions,

$$\varphi_i = \phi_{\mathbf{X}_i} \chi_i \tau_i, \quad (2)$$

$$\phi_{\mathbf{X}_i}(\mathbf{r}_j) = \left(\frac{2\nu}{\pi}\right)^{3/4} \exp[-\nu(\mathbf{r}_j - \mathbf{X}_i)^2], \quad (3)$$

$$\chi_i = \left(\frac{1}{2} + \xi_i\right)\chi_\uparrow + \left(\frac{1}{2} - \xi_i\right)\chi_\downarrow. \quad (4)$$

Here $\phi_{\mathbf{X}_i}$ and χ_i are the spatial and spin functions, respectively, and τ_i is the isospin function fixed to be proton or neutron. The width parameter $\nu = 0.19 \text{ fm}^{-2}$ is used to minimize the ground state energy of ^{12}C . The parameters $\mathbf{Z} \equiv \{\mathbf{X}_1, \dots, \mathbf{X}_A, \xi_1, \dots, \xi_A\}$ indicate Gaussian centroids and spin orientations, which are treated as variational parameters. In order to obtain the AMD wave function for the lowest J^π state, the VAP is done as

$$\frac{\delta}{\delta \mathbf{Z}} \frac{\langle \Phi | H | \Phi \rangle}{\langle \Phi | \Phi \rangle} = 0, \quad (5)$$

$$\Phi = P_{MK}^{J\pi} \Phi_{\text{AMD}}(\mathbf{Z}), \quad (6)$$

where $P_{MK}^{J\pi}$ is the spin-parity projection operator. For the second and third J^π states, the VAP is done for the component orthogonal to the lower J^π states. One of the advantages of the AMD is that the model is free from *a priori* assumption of clusters because Gaussian centroids and spin orientations of all single-particle wave functions are independently treated, but it is able to describe the cluster formation as well as the cluster breaking. However, in general, the AMD calculation with a limited number of basis wave functions is not necessarily enough for a detailed description of large amplitude inter-cluster motion in developed cluster states.

In order to improve this problem of the AMD, we explicitly include the 3α -cluster wave functions with the GCM. We express various 3α -cluster configurations with the Brink-Bloch cluster wave functions [51] and superpose them with the AMD+VAP wave functions. In what follows, we call the AMD+VAP calculation without the 3α -cluster GCM just the ‘‘AMD’’, and that with the 3α -cluster GCM ‘‘AMD+GCM’’. In the former calculation, we superpose 23 configurations of the AMD wave functions adopted in Ref. [29]. In the latter, 150 configurations of the 3α -cluster are included with the AMD wave functions as done in Ref. [39].

As inputs from the structure calculations to the microscopic CC calculation of the α scattering, the matter and transition densities of ^{12}C are calculated using the AMD and AMD+GCM wave functions. The transition strengths and form factors are also calculated and compared with experimental data determined by the γ -decay lifetimes and electron scattering. The definitions of the densities, strengths, and form factors are given in Appendixes A and B.

III. MICROSCOPIC COUPLED-CHANNEL CALCULATION WITH g -MATRIX FOLDING MODEL

The CC potentials are microscopically derived by folding the g -matrix effective NN interaction with the target and projectile densities. We use the Melbourne g -matrix interaction [48], which has been successfully used in describing the α -nucleus scattering [47, 52]. The α -nucleus potential is calculated with an extended nucleon-nucleus folding (NAF) model. In this model, first, the nucleon-nucleus CC potentials are obtained by the single folding model using the transition densities of the target nucleus, and then these potentials are folded with the ${}^4\text{He}$ one-body density. For the ${}^4\text{He}$ density, we employ the one-range Gaussian density given by Eq. (24) of Ref. [53]. The validity of the NAF model for the α elastic scattering is discussed through the comparison with the so-called target density approximation (TDA) in Ref. [52]. The NAF model is found to well simulate the TDA model and reasonably describe the α elastic scattering on ${}^{58}\text{Ni}$ and ${}^{208}\text{Pb}$ in a wide range of incident energies of $E_\alpha = 20\text{--}200$ MeV/u.

It is concluded in Ref. [52] that the TDA model has a clear theoretical foundation in view of the multiple scattering theory and is superior to the conventional frozen density approximation (FDA) in describing the α elastic scattering. Later, the TDA model has successfully been applied to the ${}^3\text{He}$ elastic scattering [54] on ${}^{58}\text{Ni}$ and ${}^{208}\text{Pb}$, and to the α inelastic scattering on ${}^{12}\text{C}$ [47]. The NAF model adopted in this study will be interpreted as a practical alternative to the TDA model. Nevertheless, there remain some model uncertainties in the reaction calculation, at backward angles in particular.

In the default CC calculation of the elastic and inelastic α scattering, we adopt the nine states, $0_{1,2,3}^+$, $2_{1,2}^+$, $4_{1,2}^+$, 1_1^- , and 3_1^- , of the target ${}^{12}\text{C}$ nucleus, with the matter and transition densities obtained with the AMD and AMD+GCM calculations, which are scaled so as to reproduce the observed transition strengths to reduce possible ambiguity from the structure calculations. For the excitation energies of ${}^{12}\text{C}$, we use the experimental values listed in Table I. In the calculation of the 1_2^- cross sections with the AMD+GCM, we adopt 13 states including four states, 2_3^+ (12.0 MeV), 2_4^+ (15.44 MeV), 1_2^- , and 3_2^- , additionally to the above-mentioned nine states. For the 1_2^- and 3_2^- states, which are theoretically predicted in the AMD+GCM calculation, we choose the excitation energies $E_x = 14$ MeV and $E_x = 13$ MeV, respectively.

For comparison, we also perform the CC calculation with the RGM density of ${}^{12}\text{C}$ taken from Ref. [9], which have been used in reaction calculations of the α scattering on ${}^{12}\text{C}$ [41–43, 45, 47]. In the CC calculation with the RGM density, we adopt five states, the $0_{1,2}^+$, $2_{1,2}^+$, and 3_1^- , of ${}^{12}\text{C}$. We do not include the 0_3^+ state of the RGM calculation because it does not correspond to the physical 0_3^+ state observed around 10 MeV.

IV. STRUCTURE PROPERTIES OF ${}^{12}\text{C}$

In this section, we show structure properties such as radii, transition strengths, and form factors of the ground and excited states of ${}^{12}\text{C}$ obtained with the AMD and AMD+GCM calculations. For comparison, we also show the RGM result of the 3α -cluster model from Ref. [9]. Note that, in these structure calculations, there are differences not only in the model wave functions but also in the effective nuclear interactions. The MV1 central interaction [55] with the Majorana parameter $M = 0.62$ and the G3RS [56, 57] spin-orbit interactions with the strength parameters $u_1 = -u_2 = 3000$ MeV are used in the AMD and AMD+GCM calculations, whereas the Volkov No.2 central interaction [58] with $M = 0.59$ is used in the RGM calculation.

A. Energy spectra and radii of ${}^{12}\text{C}$

In Table I, excitation energies and root-mean-square (rms) proton radii of the ground and excited states of ${}^{12}\text{C}$ obtained with the structure model calculations of the AMD, AMD+GCM, and RGM are listed together with the experimental data. The AMD and AMD+GCM calculations well reproduce the energy spectra except for those of the $4_{1,2}^+$ states, which are somewhat underestimated. Compared to the RGM, the better reproduction of the 2_1^+ excitation energy is obtained in these two calculations because of the α -cluster breaking effect. For the nuclear size of the excited states, three calculations show a trend similar to each other. Namely, relatively small sizes are obtained for the 2_1^+ and 4_1^+ states in the ground band, whereas much larger sizes than the ground state are obtained for the developed cluster states such as $0_{2,3}^+$, 1_1^- , 2_2^+ , 3_1^- , and 4_2^+ states. Quantitatively, the AMD+GCM tends to give slightly larger sizes for the developed cluster states than the AMD because of the large amplitude cluster motion. Compared with the two calculations, the RGM shows almost consistent sizes for the 0_2^+ and 2_2^+ states, but a much smaller size for the 3_1^- state than other two calculations. In the density profile, one can see qualitatively similar behavior in the three calculations, but quantitatively, some differences are found in the central and tail parts of the density. Comparison of the density between three calculations is given in Fig. 6 of Appendix A. These differences in the nuclear size and density can be regarded as model ambiguity from structure calculations.

B. Transition strengths and scaling factors of ${}^{12}\text{C}$

The transition strengths of ${}^{12}\text{C}$ obtained with the AMD, AMD+GCM, and RGM calculations are listed in Table II together with the experimental data. The calculated transition strengths are in reasonable agreement with the experimental data though the agreement

TABLE I: Excitation energies E_x (MeV) and rms proton radii R_p (fm) of ^{12}C obtained with the AMD and AMD+GCM calculations. Theoretical values of the RGM from Ref. [9] are also shown. The experimental energies are taken from Ref. [59]. The experimental value of the rms proton radius of the ground state is deduced from the experimental charge radius measured by the electron scattering [60].

	exp		AMD		AMD+GCM		RGM	
	E_x	R_p	E_x	R_p	E_x	R_p	E_x	R_p
0_1^+	0.0	2.33	0.0	2.53	0.0	2.54	0.0	2.40
0_2^+	7.65		8.1	3.27	7.3	3.62	7.74	3.47
0_3^+	10.3		10.7	3.98	10.0	3.92		
1_1^-	10.84		12.6	3.42	10.7	3.87		
2_1^+	4.44		4.5	2.66	4.2	2.67	2.77	2.38
2_2^+	9.87		10.6	3.99	9.5	4.09	9.38	3.85
3_1^-	9.64		10.8	3.13	9.3	3.49	8.14	2.77
4_1^+	13.3		10.9	2.71	10.5	2.79		
4_2^+	14.08		12.6	4.16	11.6	4.22		

is not perfect. In order to reduce ambiguity from the structure model calculation, we introduce the scaling factor $f_{\text{tr}} = \sqrt{B_{\text{exp}}(E\lambda)/B_{\text{cal}}(E\lambda)}$ (square root of the $B(E\lambda)$ ratio of the experimental value to the theoretical one) and scale the calculated transition densities as $\rho^{(\text{tr})}(r) \rightarrow f_{\text{tr}}\rho^{(\text{tr})}(r)$ to fit the experimental $E\lambda$ transition strengths for the use of the α scattering calculation. The value of f_{tr} for each transition is shown in Table II. For the $1_1^- \rightarrow 0_1^+$ transition, we determine the scaling factor f_{tr} by adjusting the calculated charge form factors to the experimental data measure by the electron scattering [61]. For other transitions with no data of the $E\lambda$ transition strengths, we set $f_{\text{tr}} = 1$ and use the calculated transition densities without the scaling, but the model ambiguity remains. For instance, for the $0_3^+ \rightarrow 0_1^+$ transition, the predicted $B(E0)$ value of the AMD+GCM is twice as large as that of the AMD. Also in the transitions of $2_2^+ \rightarrow 0_2^+$ and $2_2^+ \rightarrow 0_3^+$, which are important for the band assignment of these cluster states near the 3α threshold energy, there are significant differences in the predicted $E2$ strengths between the AMD, AMD+GCM, and RGM calculations. Even though the transition strengths are adjusted to the experimental data with the scaling factor, some differences can be seen in detailed behavior of the calculated transition densities between the AMD (or AMD+GCM) and RGM. In Appendix A, we compare the scaled transition densities $f_{\text{tr}}\rho^{(\text{tr})}(r)$ between three calculations.

In Fig. 1, the theoretical form factors for electron elastic and inelastic scattering of the AMD and AMD+GCM are shown compared with the experimental data. The calculated squared form factors after the scaling with the factor f_{tr}^2 reasonably agree with the experimental data.

V. α SCATTERING CROSS SECTIONS

The cross sections of the $^{12}\text{C}(\alpha, \alpha')$ reaction at incident energies of $E_\alpha = 130$ MeV, 172.5 MeV, 240 MeV, and 386 MeV are calculated by the CC calculation with the g -matrix folding potentials using the theoretical transition densities scaled by the factor f_{tr} . The cross sections obtained with the AMD, AMD+GCM, and RGM densities are discussed in comparison with experimental data. The cross sections obtained by the DWBA calculation are also shown to discuss the CC effect.

A. Cross sections with the AMD and AMD+GCM

In Figs. 2 and 3, the calculated cross sections with the AMD (solid lines) and AMD+GCM (dashed lines) are shown together with experimental data. The cross sections obtained by the DWBA calculation with the AMD are also shown by the dotted lines.

The obtained cross sections are qualitatively similar to each other between the AMD and AMD+GCM. These calculations reasonably reproduce the cross sections for the elastic scattering and the inelastic scattering to the $0_{2,3}^+$, 2_1^+ , 1_1^- , and 3_1^+ states. It should be stressed again that the present microscopic CC calculation with the g -matrix folding potentials contains no adjustable parameter except for the scaling factor to fit the data of the electric transition strengths, $B(E\lambda)$. It indicates the applicability of the present model for the α scattering on ^{12}C in this energy region of $E_\alpha = 130$ –400 MeV.

In the 0_2^+ cross sections, one can see that the amplitudes of the first and second peaks are reproduced well, and there is no overshooting problem of the 0^+ cross sections for this state as in Ref. [47]. In the 0_3^+ inelastic cross sections, two calculations of the AMD and AMD+GCM show a slight difference in the absolute amplitude: the AMD+GCM shows about 1.5 times larger cross sections than the AMD because of the larger $E0$ strength for the direct transition $0_1^+ \rightarrow 0_3^+$, but both reasonably describe the experimental cross sections taken at $E_\alpha = 240$ MeV [38]. It should be remarked that the data corresponding to the broad resonance around 10.3 MeV, and it can contain two 0^+ states as reported recently [36].

For the 2_1^+ cross sections, there is no difference between the AMD and AMD+GCM. Both reproduce the cross sections with comparable quality to the elastic scattering. As for the 3_1^- cross sections, the AMD and AMD+GCM show a quantitative difference in the absolute amplitude even though the $E3$ transition strength is adjusted to the experimental value in both cases. The AMD+GCM gives somewhat smaller cross sections than the AMD. A possible reason for this is the larger radius of the 3_1^- state in the AMD+GCM, which may cause stronger absorption than in the AMD.

For the 1_1^- cross sections, the AMD and AMD+GCM results are consistent with each other, and both are in reasonable agreement with the experimental data at

TABLE II: The transition strengths $B(E\lambda)$ of ^{12}C calculated with the AMD, AMD+GCM, and RGM. For the $1_1^- \rightarrow 0_1^+$ transition, a quarter of the isoscalar dipole transition strength $B(\text{IS}\lambda)/4$ is shown. The scaling factors $f_{\text{tr}} = \sqrt{B_{\text{exp}}(E\lambda)/B_{\text{cal}}(E\lambda)}$ determined by the ratio of the experimental strength $B_{\text{exp}}(E\lambda)$ and the calculated strength $B_{\text{cal}}(E\lambda)$ are also shown. The experimental $B(E\lambda)$ are taken from Ref. [59]. ^aThe updated value of $B(E2 : 2_2^+ \rightarrow 0_1^+)$ from Ref [3] by the reanalysis of the data in Ref. [62]. ^bThe f_{tr} value for the $1_1^- \rightarrow 0_1^+$ transition is determined by adjusting the charge form factor to the electron scattering data [61]. The units of the transition strengths are $e^2 \text{ fm}^4$ for $B(E0)$, fm^6 for $B(\text{IS}1)$, and $e^2 \text{ fm}^{2\lambda}$ for other $B(E\lambda)$.

	exp		AMD		AMD+GCM		RGM	
	$B(E\lambda)$	(error)	$B(E\lambda)$	f_{tr}	$B(E\lambda)$	f_{tr}	$B(E\lambda)$	f_{tr}
$E2 : 2_1^+ \rightarrow 0_1^+$	7.59	(0.42)	8.53	0.94	9.09	0.91	9.31	0.90
$E0 : 0_2^+ \rightarrow 0_1^+$	29.2	(0.2)	43.5	0.82	43.3	0.82	43.8	0.82
$E2 : 0_2^+ \rightarrow 2_1^+$	13.5	(1.4)	25.1	0.73	24.1	0.75	5.6	1.56
$E2 : 2_2^+ \rightarrow 0_1^+$	1.57 ^a	(0.13)	0.39	1.99	0.49	1.93	2.48	0.80
$E2 : 3_1^- \rightarrow 1_1^-$			40.7	1	79.0	1		
$E0 : 0_3^+ \rightarrow 0_1^+$			5.2	1	10.0	1		
$\text{IS}1 : 1_1^- \rightarrow 0_1^+$			2.6	1.57 ^b	2.4	1.93 ^b	5.7	1
$\text{IS}1 : 1_2^- \rightarrow 0_1^+$					1.5	1		
$E3 : 3_1^- \rightarrow 0_1^+$	103	(17)	71	1.20	71	1.20	125	0.91
$E4 : 4_1^+ \rightarrow 0_1^+$			733	1	995	1	655	1
$E3 : 3_1^- \rightarrow 0_2^+$			428	1	1210	1	228	1
$E2 : 2_2^+ \rightarrow 0_2^+$			102	1	182	1	212	1
$E2 : 2_2^+ \rightarrow 0_3^+$			309	1	223	1		

$E_\alpha = 240$ MeV. Because the scaled transition density can reproduce both the electric scattering and α scattering data, we can estimate the IS dipole transition strength as $B(\text{IS}1; 1_1^- \rightarrow 0_1^+)/4 = 6\text{--}9 \text{ fm}^6$.

The 2_2^+ state is the newly discovered state by α inelastic scattering and β -decay experiments [3, 36, 37]. The predicted cross sections of the 2_2^+ state are much smaller than the 2_1^+ state consistently with the weak $E2$ transition from the 0_1^+ , a small $B(E2; 2_2^+ \rightarrow 0_1^+)$, because this state is the cluster state and has the strong $E2$ transitions not to the ground state but to the 0_2^+ and 0_3^+ states. In Fig. 4, we compare the incoherent sum of the 2_2^+ and 0_3^+ cross sections at 386 MeV compared with the experimental sum of the 2_2^+ (9.84) MeV and 0_3^+ (9.93 MeV) reported in Ref. [36]. The 2_2^+ and 0_3^+ cross sections at 240 MeV are also shown together with the experimental 0_3^+ cross sections. In the calculation, the 0_3^+ and 2_2^+ cross sections describe respectively the first and second peaks, and both contribute to the third peak of the summed cross sections. This result is similar to the experimental MDA analysis [36] and the theoretical calculation of Ref. [45], where the optical potentials have been phenomenologically tuned to reproduce the experimental cross sections. In the reproduction of the experimental data, the AMD result seems to be favored rather than the AMD+GCM, though quality of the reproduction is not satisfactory to conclude it.

For the 1_2^- , and 4_2^+ states, there are no available data and the calculated cross sections are theoretical predictions. As discussed in Ref. [40], the predicted 1_2^- is a toroidal dipole state and contributes to the isoscalar

dipole strengths in the low-energy region below the giant dipole resonance. In the α scattering experiment at 240 MeV [38], the significant isoscalar dipole strength around 15 MeV has been observed in the MDA, and it is a candidate for the predicted toroidal state of the 1_2^- .

TABLE III: References for experimental differential cross sections of the α scattering on ^{12}C at incident energies of $E_\alpha = 130$ MeV, 172.5 MeV, 240 MeV, and 386 MeV. ^aThe excitation energy of the 0_3^+ state (the broad resonance around 10 MeV) is 10.3 MeV in Ref. [38] and 9.93 MeV in Ref. [36]. ^bThe sum of the cross sections of the 2_2^+ (9.84 MeV) and 0_3^+ (9.93 MeV).

$J_f^\pi (E_x)$	130 MeV	172 MeV	240 MeV	386
$0_1^+(0.00)$	[46]	[50],[49]	[38]	[36]
$2_1^+(2.44)$	[46]	[50]	[38]	[36]
$0_2^+(7.65)$	[46]	[50]	[38]	[36],[46]
$0_3^+(10.3^a)$			[38]	[36] ^b
$2_2^+(9.84)$				[36] ^b
$3_1^-(9.64)$	[46]	[50]	[38]	[36],[46]
$1_1^-(10.84)$	[46]		[38]	
$4_1^+(14.0)$		[50]		

B. Coupled-channel effects

Let us discuss the CC effect in comparison with the DWBA calculation shown in Figs. 2 and 3.

For the 0_1^+ and 2_1^+ cross sections, the results are almost consistent between the DWBA and CC calculations, and only a slight difference can be seen at large scattering angles. For other states, the CC effect is significant, in particular, at low incident energies, and still remains even at $E_\alpha = 386$ MeV. In the 0_2^+ , 2_2^+ , and 3_1^- cross sections, the absolute amplitudes are reduced by the CC effect. Compared with the DWBA calculation, the peak positions are almost unchanged but dips are somewhat smeared in the CC calculation for the 0_2^+ and 2_2^+ . The CC effect on the 0_2^+ cross sections is dominantly contributed by the $\lambda = 2$ transitions with the 2_1^+ and 2_2^+ and $\lambda = 3$ transition with the 3_1^- . The CC effect on the 2_2^+ cross sections turn out to be through the $\lambda = 2$ transition with the 0_2^+ and the $\lambda = 3$ transition with the 3_1^- ,

For the 0_3^+ cross sections, the CC effect gives an opposite contribution, namely, it enhances the cross sections. Consequently, the calculated 0_3^+ cross sections are the same order as the 0_2^+ cross sections even though the monopole transition strength to the 0_3^+ is about one order smaller than the strength to the 0_2^+ . This result indicates that the 0^+ cross sections do not scale with the monopole transition strengths contrary to the naive expectation of the linear scaling, which is often assumed in the experimental determination of isoscalar transition strengths with the DWBA analysis of the α inelastic scattering.

Further significant CC effects are found in the 1_1^- , 4_1^+ , and 4_2^+ cross sections. For these states, not only the absolute amplitude but also the diffraction pattern of the cross sections are affected. For the 1_1^- cross sections, the absolute values are reduced and the first and second peak positions are shifted to the forward angle by the CC effect, which is essential to describe the experimental cross sections at 130 MeV. The dominant contribution to the 1_1^- cross sections is the coupling with the 3_1^- state through the strong $\lambda = 2$ transition. Compared with the 1_1^- case, the CC effect in the 1_2^- cross sections is not so large. The present calculation predicts almost the same amplitude of the 1_2^- cross sections as the 1_1^- cross sections even though the isoscalar dipole transition strength is weaker in the $1_2^- \rightarrow 0_1^+$ than in the $1_1^- \rightarrow 0_1^+$ as shown in Table II.

For the 4_1^+ and 4_2^+ states, the cross sections are strongly influenced by the channel coupling. For the 4_1^+ cross sections, the present CC calculation reproduces the absolute amplitude but does not describe the diffraction pattern of the experimental cross sections.

C. Cross sections with the RGM

Figure 5 shows the cross sections obtained with the RGM together with the AMD result as well as the experi-

mental data. Some differences can be seen in the inelastic cross sections between the RGM and AMD. The RGM shows larger cross sections for the 3_1^- than the AMD, and tends to overestimate the experimental data. The absorption may be too weak in the RGM because of the smaller radius of the 3_1^- state than the AMD result. For the 0_2^+ cross sections, the peak and dip structures are smeared by the stronger CC effect in the RGM result, and the reproduction of the experimental data becomes somewhat worse than the AMD. Also in the 2_2^+ cross sections, the strong CC effect smears the diffraction patterning in the RGM result.

VI. SUMMARY

The α elastic and inelastic scattering on ^{12}C was investigated by the microscopic CC calculation with the g -matrix folding model. The α -nucleus CC potentials are derived by folding the Melbourne g -matrix NN interaction with the transition densities calculated with the microscopic structure models of the AMD and AMD+GCM.

The present calculation reasonably reproduces the differential cross sections of the α scattering at incident energies of $E_\alpha = 130$ MeV, 172.5 MeV, 240 MeV, and 386 MeV with no adjustable parameter except for the scaling factor to fit the data of the electric transition strengths, $B(E\lambda)$. The calculation successfully describes the absolute amplitude of the 0_2^+ cross sections and does not encounter the overshooting problem of the 0^+ cross sections, the so-called missing monopole strength. This result is consistent with the preceding work by Minomo and Ogata [47] using the RGM transition densities. Moreover, the present calculation reproduces the 0_3^+ cross sections and also describes the sum of the 0_3^+ and 2_2^+ cross sections. In comparison with the DWBA calculation, the CC effect on the inelastic scattering cross sections except for the 2_1^+ cross sections is found to be significant, in particular, at low incident energies, and still remains even at $E_\alpha = 386$ MeV.

It was found that the absolute values of the inelastic cross sections do not necessarily scale linearly with the transition strength, because it is sensitively influenced by the coupling with other channels and also by the radius of the excited state. This may be a characteristic aspect of the α scattering on ^{12}C , in which cluster states near the threshold energy have larger radii than the states in the ground band states and there exist strong transitions between each other. It indicates that reliable microscopic calculation of α scattering is needed to extract quantitative information on the transition strengths from the α inelastic scattering. It should be remarked that such calculation may reveal also properties of the coupling between excited states that cannot be studied if the DWBA picture holds. The α inelastic cross sections contain rich information on the excited states of ^{12}C through the CC effect. The present model has been proved to be appli-

cable to the α elastic and inelastic scattering for cluster states and can be a powerful tool for investigation of not only the isoscalar monopole and dipole transitions but also transitions between excited states for general stable and unstable nuclei.

Nevertheless, there still remain problems in an accurate reproduction of the cross sections. There is no ambiguity for the known transitions because the theoretical transition densities are scaled to fit existing data of the transition strengths. However, for unknown transitions, in particular, transitions between excited states, model ambiguity remains in the structure calculations. Another unknown factor is the nuclear size of the excited states. Further reliable structure calculations are needed to reduce the ambiguity from these factors. Also in the reaction part, further improvements can be considered. For example, treatments of the density dependences of the g -matrix effective interactions and a possible contribution of the three-nucleon force effect should be tested more carefully for better reproduction of the scattering cross sections, those at backward angles in particular.

Acknowledgments

The computational calculations of this work were performed by using the supercomputer in the Yukawa Institute for theoretical physics, Kyoto University. This work was supported in part by Grants-in-Aid of the Japan Society for the Promotion of Science (Grant Nos. JP26400270, JP18K03617, and JP16K05352).

Appendix A: Matter and transition densities

The density operator of nuclear matter is

$$\rho(\mathbf{r}) = \sum_k \delta(\mathbf{r} - \mathbf{r}_k). \quad (\text{A1})$$

The transition density for the transition $|i\rangle \rightarrow |f\rangle$ is given as $\rho_{i \rightarrow f}^{(\text{tr})}(\mathbf{r}) \equiv \langle f | \rho(\mathbf{r}) | i \rangle$, and its λ th moment is obtained from the multipole decomposition,

$$\begin{aligned} \rho_{i \rightarrow f}^{(\text{tr})}(\mathbf{r}) &= \frac{1}{\sqrt{2J_f + 1}} \sum_{\lambda} \rho_{\lambda; i \rightarrow f}^{(\text{tr})}(r) \\ &\times \sum_{\mu} Y_{\lambda\mu}^*(\hat{\mathbf{r}}) (J_i M_i \lambda \mu | J_f M_f), \end{aligned} \quad (\text{A2})$$

where J_i and M_i (J_f and M_f) are the spin quantum numbers of the initial $|i\rangle$ (final $|f\rangle$) state. It should be remarked that the transition density $\rho_{\lambda; i \rightarrow f}^{(\text{tr})}(r)$ defined here is related to the transition density $\rho_{\lambda; i \rightarrow f}^{(\text{tr:K})}(r)$ used by Kamimura in Ref. [9] as

$$\rho_{\lambda; i \rightarrow f}^{(\text{tr:K})}(r) = \frac{1}{\sqrt{2J_f + 1}} \rho_{\lambda; i \rightarrow f}^{(\text{tr})}(r). \quad (\text{A3})$$

The matter density $\rho(r)$ of the state $|i\rangle$ is related to the diagonal component of the $\lambda = 0$ transition density as

$$\rho(r) = \frac{1}{\sqrt{4\pi}} \rho_{0; i \rightarrow i}^{(\text{tr})}(r). \quad (\text{A4})$$

The volume integral of the matter density equals to the mass number A as

$$A = \int 4\pi r^2 \rho(r) dr. \quad (\text{A5})$$

The matter and transition densities obtained with the AMD, AMD+GCM, and RGM calculations are shown in Figs. 6 and 7, respectively.

Appendix B: Definitions of transition operators, strengths, and form factors

For the rank $\lambda \neq 0, 1$, the isoscalar transition operator is given as

$$M_{\text{IS}\lambda}(\mu) \equiv \int d\mathbf{r} \rho(\mathbf{r}) r^{\lambda} Y_{\lambda\mu}(\hat{\mathbf{r}}), \quad (\text{B1})$$

and the matrix element is related to the transition density as

$$\langle f | M_{\text{IS}\lambda} | i \rangle = \int dr r^2 r^{\lambda} \rho_{\lambda; i \rightarrow f}^{(\text{tr})}(r). \quad (\text{B2})$$

In the present calculation, the electric transitions are calculated by assuming the mirror symmetry because the symmetry breaking in the initial and final states are negligibly small. The $E\lambda$ transition strength is given as

$$B(E\lambda) = \frac{e^2}{4} \frac{1}{2J_i + 1} |\langle f | M_{\text{IS}\lambda} | i \rangle|^2, \quad (\text{B3})$$

where the factor of $\frac{1}{4}$ comes from the mirror symmetry assumption. For the $\lambda = 0$ case, the $E0$ transition operator, matrix elements, and strengths are given as

$$M_{\text{ISO}} \equiv \int d\mathbf{r} \rho(\mathbf{r}) r^2, \quad (\text{B4})$$

$$\langle f | M_{\text{ISO}} | i \rangle = \sqrt{4\pi} \int dr r^2 r^{\lambda+2} \rho_{\lambda; i \rightarrow f}^{(\text{tr})}(\mathbf{r}), \quad (\text{B5})$$

$$B(E0) = \frac{e^2}{4} \frac{1}{2J_i + 1} |\langle f | M_{\text{ISO}} | i \rangle|^2. \quad (\text{B6})$$

The λ th multipole component of the so-called longitudinal form factor is related to the Fourier-Bessel transform of the transition charge density $\rho_{\lambda; i \rightarrow f}^{\text{ch}}(r)$ by

$$F(q) = \frac{\sqrt{4\pi}}{Z} \frac{1}{\sqrt{2J_i + 1}} \int dr r^2 j_{\lambda}(qr) \rho_{\lambda; i \rightarrow f}^{\text{ch}}(r), \quad (\text{B7})$$

where $\rho_{\lambda; i \rightarrow f}^{\text{ch}}(r)$ is calculated by taking into account the proton charge radius.

-
- [1] H. Horiuchi, K. Ikeda, and K. Katō, *Prog. Theor. Phys. Suppl.* **192**, 1 (2012).
- [2] Y. Funaki, H. Horiuchi and A. Tohsaki, *Prog. Part. Nucl. Phys.* **82**, 78 (2015).
- [3] M. Freer and H. O. U. Fynbo, *Prog. Part. Nucl. Phys.* **78**, 1 (2014).
- [4] M. Freer, H. Horiuchi, Y. Kanada-En'yo, D. Lee and U. G. Meißner, *Rev. Mod. Phys.* **90**, 035004 (2018).
- [5] Y. Fujiwara *et al.*, *Prog. Theor. Phys. Suppl.* **68**, 29 (1980).
- [6] Y. Fukushima and M. Kamimura, *Proc. Int. Conf. on Nuclear Structure, Tokyo, 1977, edited by T. Marumori* *J. Phys. Soc. Jpn.* **44**, 225 (1978).
- [7] E. Uegaki, S. Okabe, Y. Abe and H. Tanaka, *Prog. Theor. Phys.* **57**, 1262 (1977).
- [8] E. Uegaki, Y. Abe, S. Okabe and H. Tanaka, *Prog. Theor. Phys.* **62**, 1621 (1979).
- [9] M. Kamimura, *Nucl. Phys. A* **351**, 456 (1981).
- [10] P. Descouvemont and D. Baye, *Phys. Rev. C* **36**, 54 (1987).
- [11] A. Tohsaki, H. Horiuchi, P. Schuck and G. Ropke, *Phys. Rev. Lett.* **87**, 192501 (2001).
- [12] Y. Funaki, A. Tohsaki, H. Horiuchi, P. Schuck and G. Ropke, *Phys. Rev. C* **67**, 051306 (2003).
- [13] S. I. Fedotov, O. I. Kartavtsev, V. I. Kochkin and A. V. Malykh, *Phys. Rev. C* **70**, 014006 (2004).
- [14] C. Kurokawa and K. Katō, *Nucl. Phys. A* **738**, 455 (2004).
- [15] C. Kurokawa and K. Kato, *Phys. Rev. C* **71**, 021301 (2005).
- [16] I. Filikhin, V. M. Suslov and B. Vlahovic, *J. Phys. G* **31**, 1207 (2005).
- [17] Y. Funaki, H. Horiuchi and A. Tohsaki, *Prog. Theor. Phys.* **115**, 115 (2006).
- [18] Y. Funaki, A. Tohsaki, H. Horiuchi, P. Schuck and G. Ropke, *Eur. Phys. J. A* **28**, 259 (2006).
- [19] K. Arai, *Phys. Rev. C* **74**, 064311 (2006).
- [20] S. Ohtsubo, Y. Fukushima, M. Kamimura, and E. Hiyama, *Prog. Theor. Exp. Phys.* **2013**, 073D02 (2013).
- [21] S. Ishikawa, *Phys. Rev. C* **90**, no. 6, 061604 (2014).
- [22] Y. Funaki, *Phys. Rev. C* **92**, no. 2, 021302 (2015).
- [23] Y. Kanada-En'yo, H. Horiuchi and A. Ono, *Phys. Rev. C* **52**, 628 (1995).
- [24] Y. Kanada-En'yo and H. Horiuchi, *Phys. Rev. C* **52**, 647 (1995).
- [25] Y. Kanada-En'yo, M. Kimura and A. Ono, *PTEP* **2012** 01A202 (2012).
- [26] H. Feldmeier, K. Bieler and J. Schnack, *Nucl. Phys. A* **586**, 493 (1995).
- [27] T. Neff and H. Feldmeier, *Nucl. Phys. A* **713**, 311 (2003).
- [28] Y. Kanada-En'yo, *Phys. Rev. Lett.* **81**, 5291 (1998).
- [29] Y. Kanada-En'yo, *Prog. Theor. Phys.* **117**, 655 (2007) Erratum: [*Prog. Theor. Phys.* **121**, 895 (2009)].
- [30] T. Neff and H. Feldmeier, *Nucl. Phys. A* **738**, 357 (2004).
- [31] M. Chernykh, H. Feldmeier, T. Neff, P. von Neumann-Cosel and A. Richter, *Phys. Rev. Lett.* **98**, 032501 (2007).
- [32] T. Suhara and Y. Kanada-En'yo, *Phys. Rev. C* **91**, 024315 (2015).
- [33] E. Epelbaum, H. Krebs, T. A. Lahde, D. Lee and U. G. Meißner, *Phys. Rev. Lett.* **109**, 252501 (2012).
- [34] A. C. Dreyfuss, K. D. Launey, T. Dytrych, J. P. Draayer and C. Bahri, *Phys. Lett. B* **727**, 511 (2013).
- [35] J. Carlson, S. Gandolfi, F. Pederiva, S. C. Pieper, R. Schiavilla, K. E. Schmidt and R. B. Wiringa, *Rev. Mod. Phys.* **87** 1067 (2015).
- [36] M. Itoh *et al.*, *Phys. Rev. C* **84**, 054308 (2011).
- [37] M. Freer *et al.*, *Phys. Rev. C* **86**, 034320 (2012).
- [38] B. John, Y. Tokimoto, Y.-W. Lui, H. L. Clark, X. Chen and D. H. Youngblood, *Phys. Rev. C* **68**, 014305 (2003).
- [39] Y. Kanada-En'yo, *Phys. Rev. C* **93**, 054307 (2016).
- [40] Y. Kanada-En'yo, Y. Shikata and H. Morita, *Phys. Rev. C* **97**, 014303 (2018).
- [41] S. Ohkubo and Y. Hirabayashi, *Phys. Rev. C* **70**, 041602 (2004).
- [42] M. Takashina and Y. Sakuragi, *Phys. Rev. C* **74**, 054606 (2006).
- [43] D. T. Khoa and D. C. Cuong, *Phys. Lett. B* **660**, 331 (2008).
- [44] M. Takashina, *Phys. Rev. C* **78**, 014602 (2008).
- [45] M. Ito, *Phys. Rev. C* **97**, 044608 (2018).
- [46] S. Adachi *et al.*, *Phys. Rev. C* **97**, no. 1, 014601 (2018).
- [47] K. Minomo and K. Ogata, *Phys. Rev. C* **93**, 051601 (2016).
- [48] K. Amos, P. J. Dortmans, H. V. von Geramb, S. Karataglidis, and J. Raynal, *Adv. Nucl. Phys.* **25**, 275 (2000).
- [49] S. Wiktor, C. M. Bőricke, A. Kiss, M. Rogge, P. Turek, and H. Dabrowski. 1981. *Acta Phys. Polon.*, B12, 491.
- [50] A. Kiss, C. M. Bőricke, M. Rogge, P. Turek, and S. Wiktor. *J. Phys. G* **13**, 1067 (1987).
- [51] D. M. Brink, *Proc. Int. School of Physics Enrico Fermi, Course 36, Varenna*, ed. C. Bloch (Academic Press, New York, 1966).
- [52] K. Egashira, K. Minomo, M. Toyokawa, T. Matsumoto and M. Yahiro, *Phys. Rev. C* **89**, 064611 (2014).
- [53] G. R. Satchler and W. G. Love, *Phys. Rep.* **55**, 183 (1979).
- [54] M. Toyokawa, T. Matsumoto, K. Minomo, and M. Yahiro, *Phys. Rev. C* **91**, 064610 (2015).
- [55] T. Ando, K. Ikeda, and A. Tohsaki, *Prog. Theor. Phys.* **64**, 1608 (1980).
- [56] R. Tamagaki, *Prog. Theor. Phys.* **39**, 91 (1968).
- [57] N. Yamaguchi, T. Kasahara, S. Nagata, and Y. Akaishi, *Prog. Theor. Phys.* **62**, 1018 (1979).
- [58] A. Volkov, *Nucl. Phys.* **74**, 33 (1965).
- [59] J. H. Kelley, J. E. Purcell and C. G. Sheu, *Nucl. Phys. A* **968**, 71 (2017).
- [60] I. Angeli and K. P. Marinova, *At. Data Nucl. Data Tables* **99**, 69 (2013).
- [61] Y. Torizuka *at al.*, *Phys. Rev. Lett.* **22**, 544 (1969).
- [62] W. R. Zimmerman *et al.*, *Phys. Rev. Lett.* **110**, 152502 (2013).
- [63] I. Sick and J. S. McCarthy, *Nucl. Phys. A* **150**, 631 (1970).
- [64] H. Crannel, *Phys. Rev.* **148**, 1107 (1966).
- [65] A. Nakada, Y. Torizuka, and Y. Horikawa, *Phys. Rev. Lett.* **27**, 745 (1971).

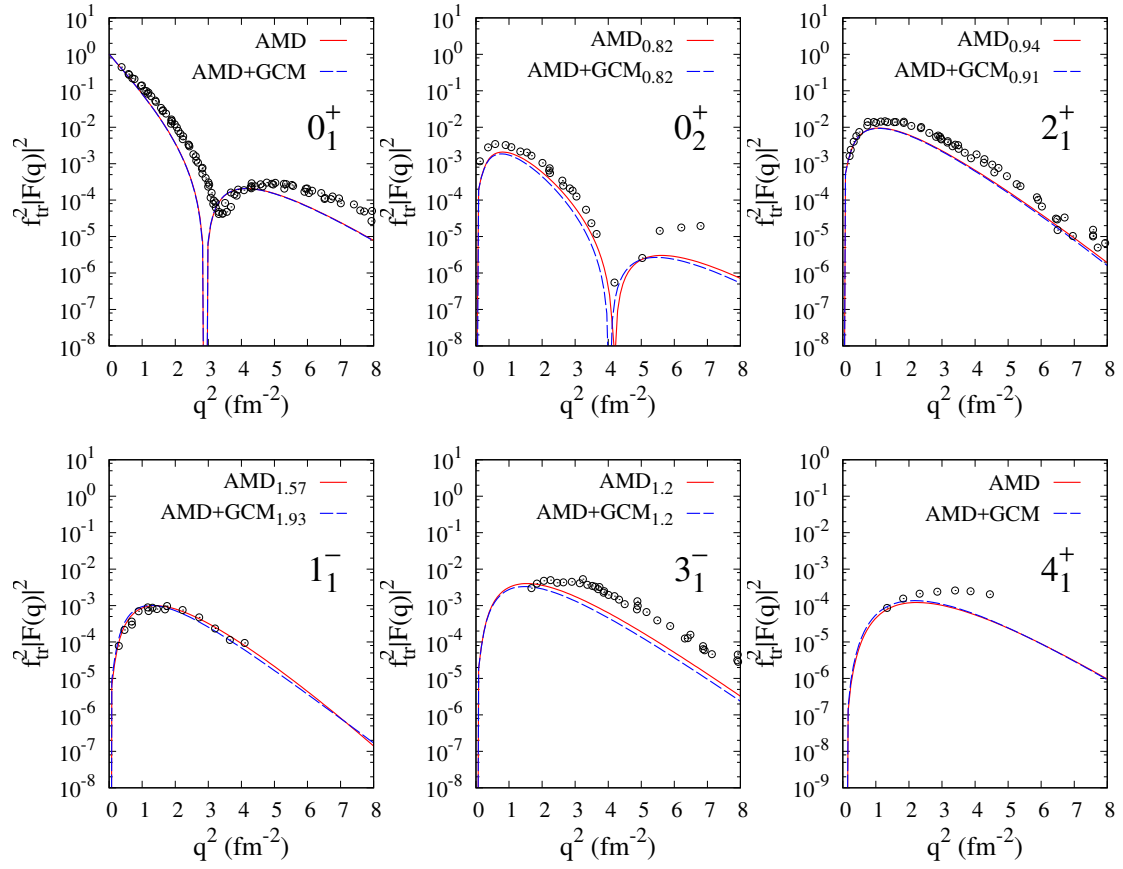


FIG. 1: Squared charge form factors of ^{12}C . The theoretical values are those obtained with AMD and AMD+GCM scaled by the factor f_{tr}^2 (labeled by AMD $_{f_{tr}}$ and AMD+GCM $_{f_{tr}}$, respectively). The experimental data are those measured by electron elastic and inelastic scattering on ^{12}C from Refs. [61, 63–65].

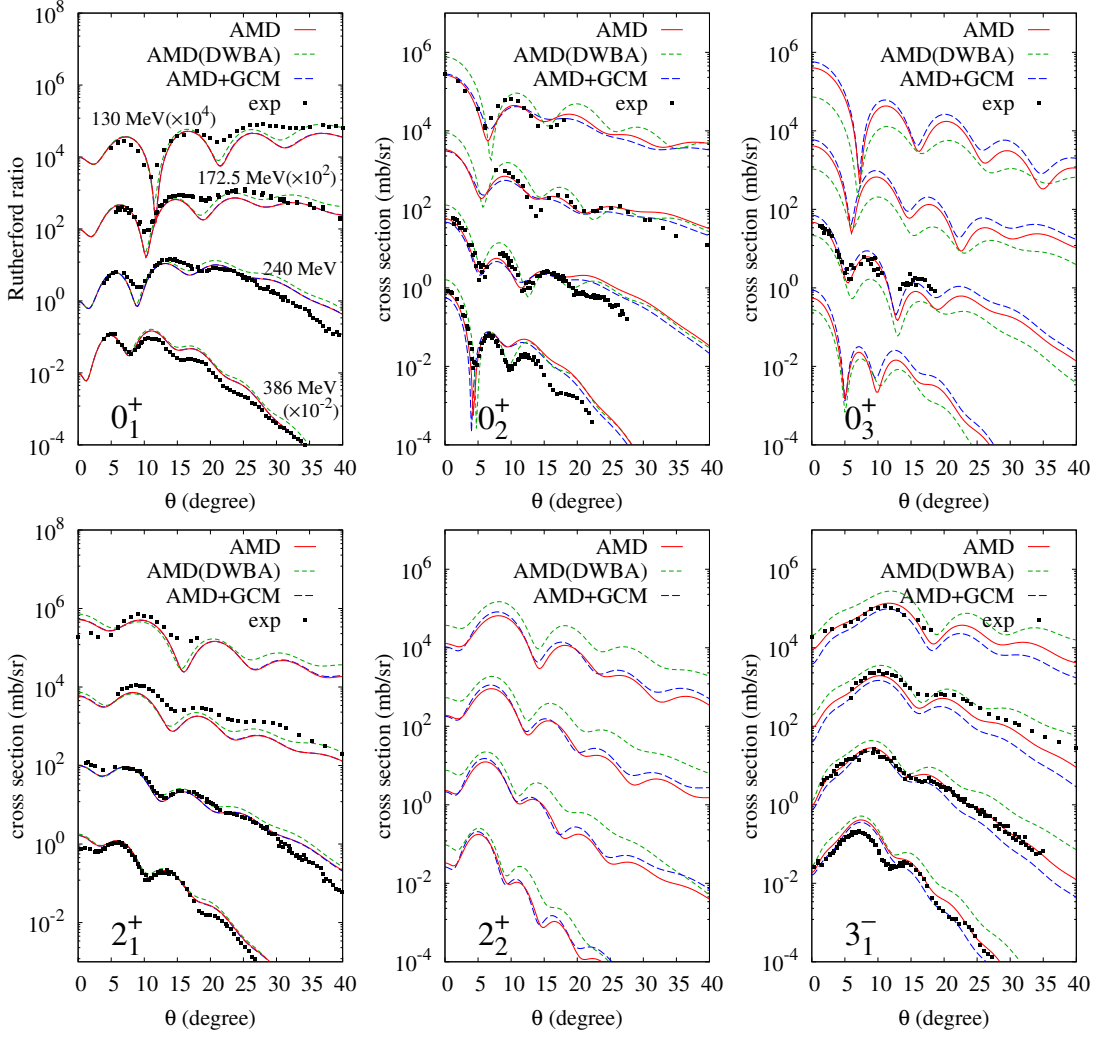


FIG. 2: α scattering cross sections on ^{12}C at $E_\alpha = 130 \text{ MeV} (\times 10^4)$, $172.5 \text{ MeV} (\times 10^2)$, 240 MeV , and $386 \text{ MeV} (\times 10^{-2})$. The differential cross sections of the $0_{1,2,3}^+$, $2_{1,2}^+$, and 3_1^- states obtained by the CC calculation with the AMD and AMD+GCM transition densities are shown. The cross sections obtained by the DWBA calculation with the AMD transition densities are also shown for comparison. The experimental data are taken from Refs. [36, 38, 46, 49, 50]. References for those data are summarized in Table III.

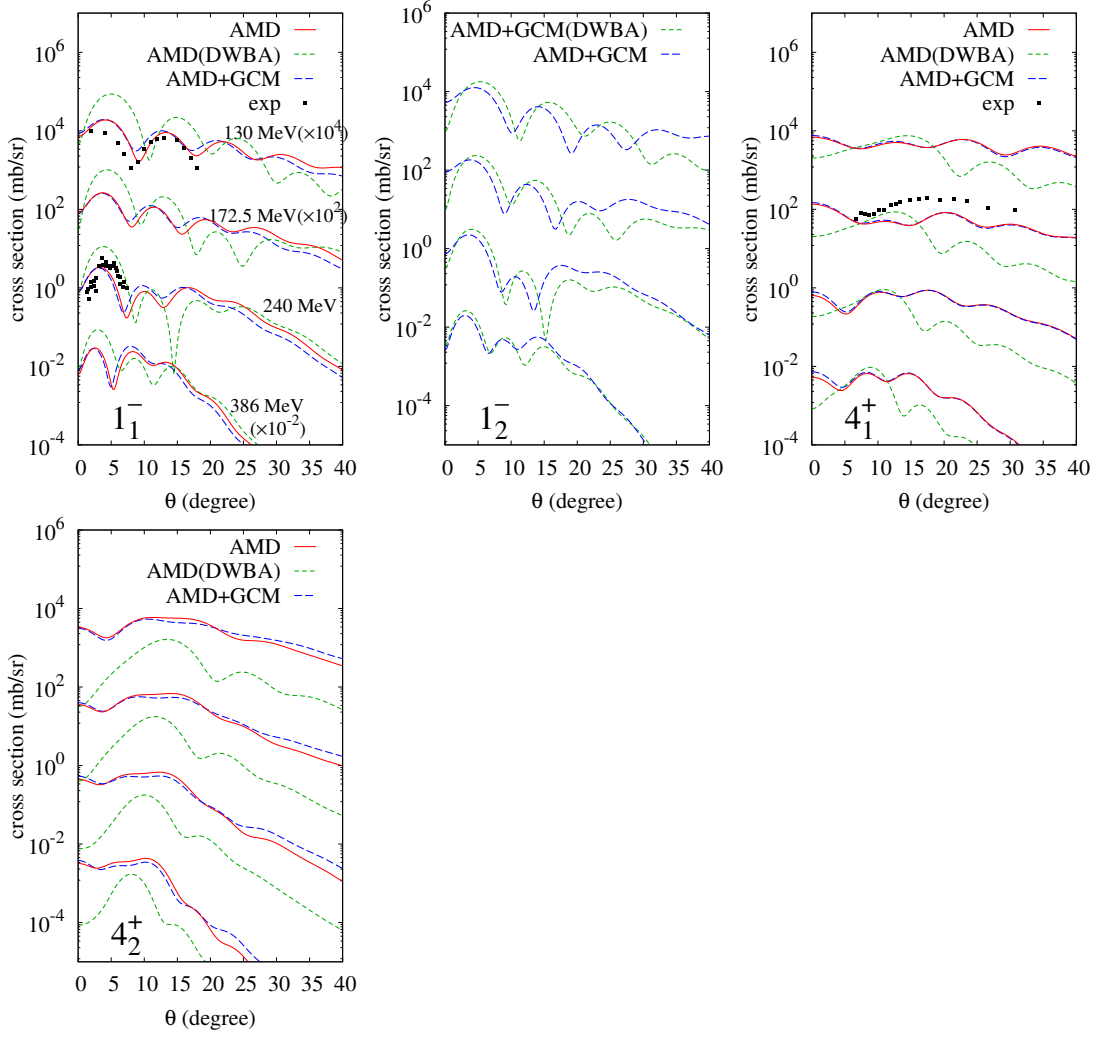


FIG. 3: Same as Fig. 2, but for the $1_{1,2}^{-}$ and $4_{1,2}^{+}$ states.

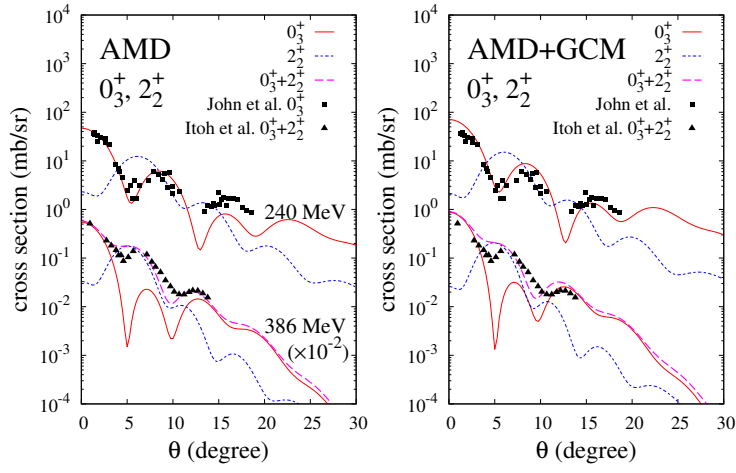


FIG. 4: 2_2^+ and 0_3^+ cross sections at $E_\alpha = 240$ MeV and 386 MeV calculated with the AMD and AMD+GCM. The incoherent sum of the 2_2^+ and 0_3^+ cross sections at 386 MeV is compared with the experimental sum of the 2_2^+ (9.84 MeV) and 0_3^+ (9.93 MeV) taken from Ref. [36]. The experimental 0_3^+ cross sections at 240 MeV are taken from Ref. [38].

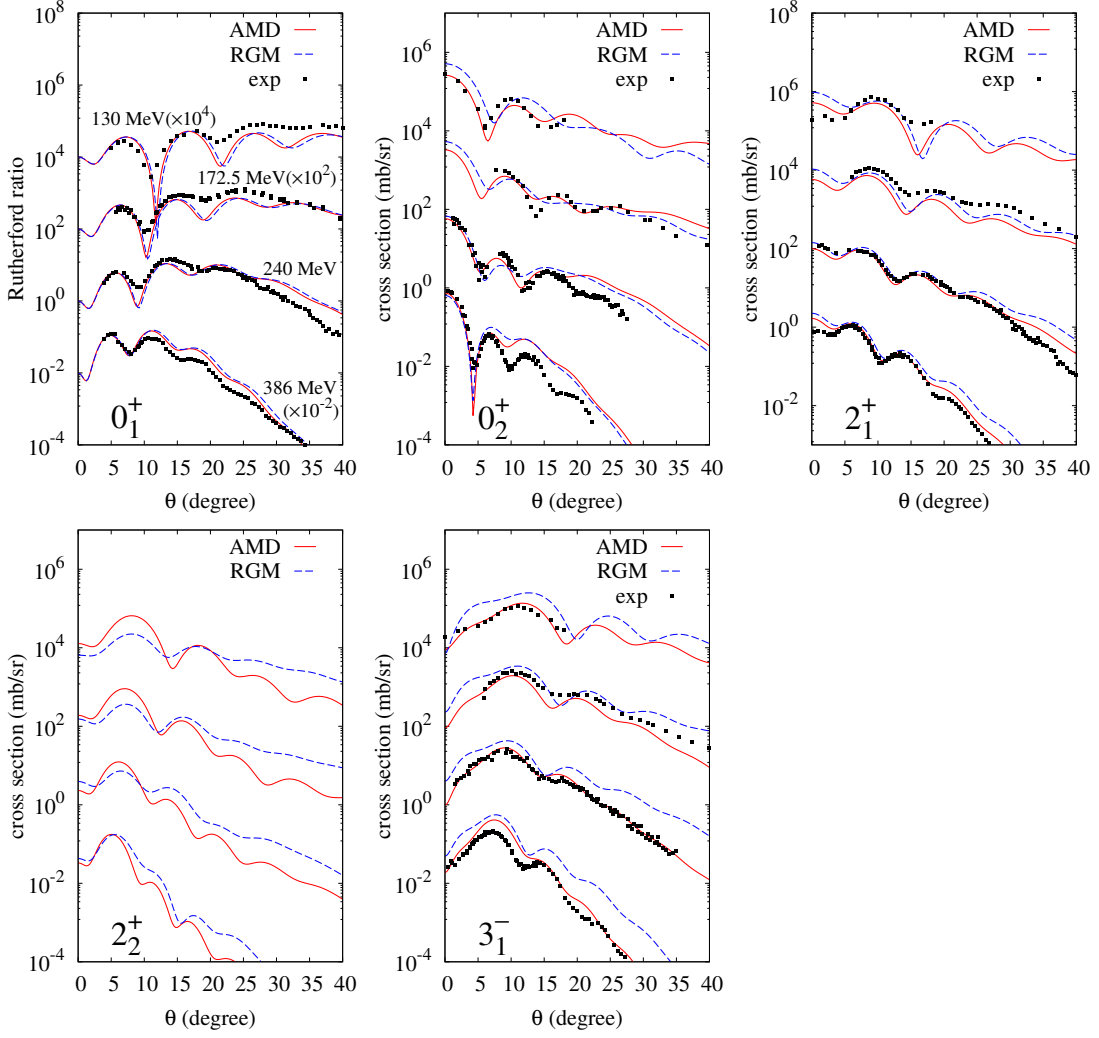


FIG. 5: α scattering cross sections on ^{12}C at $E_\alpha = 130 \text{ MeV} (\times 10^4)$, $172.5 \text{ MeV} (\times 10^2)$, 240 MeV , and $386 \text{ MeV} (\times 10^{-2})$, obtained by the CC calculation with the RGM densities compared with the AMD result. The calculated differential cross sections of the $0_{1,2}^+$, $2_{1,2}^+$, and 3_1^- states are shown. The experimental data from Refs.[36, 38, 46, 49, 50] are also shown.

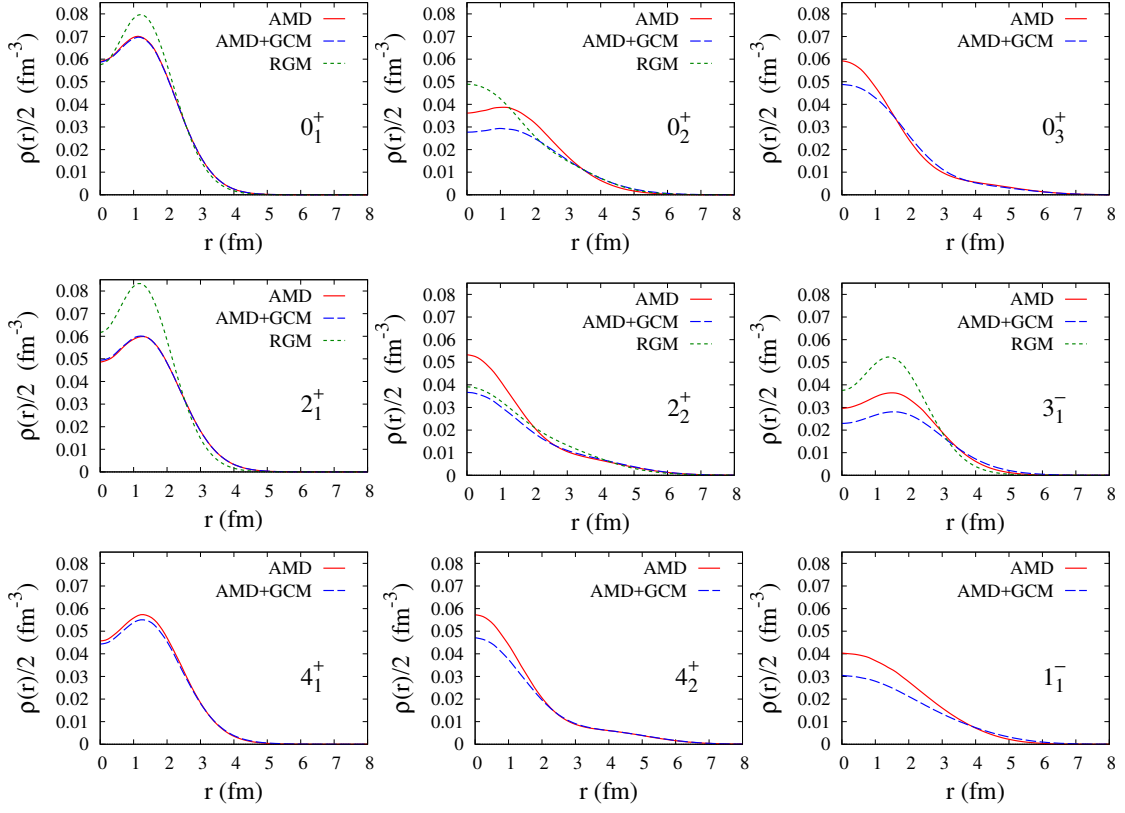


FIG. 6: proton densities $\rho_p(r) = \rho(r)/2$ of the AMD, AMD+GCM, and RGM calculations.

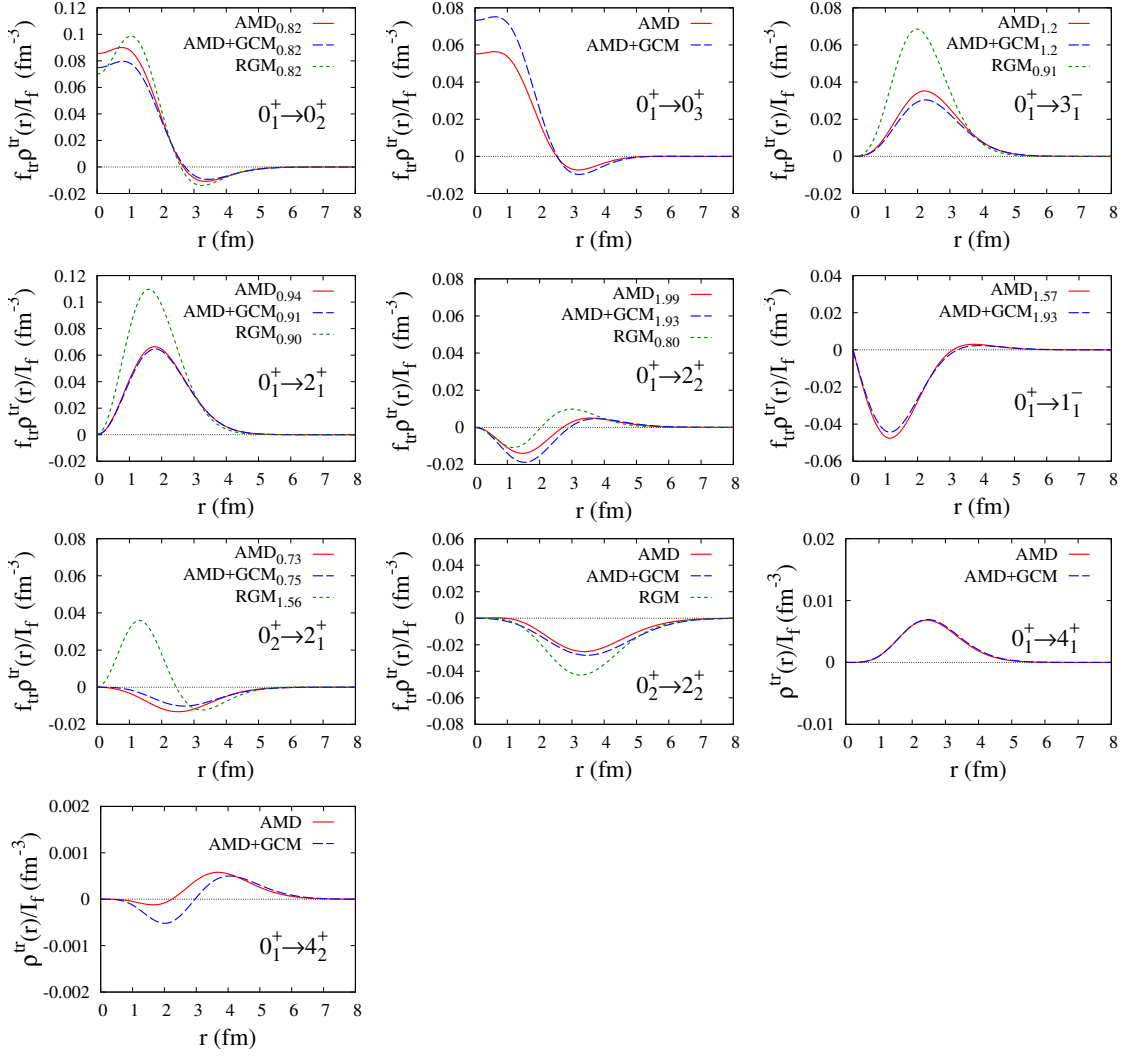


FIG. 7: transition densities $\rho^{tr}(r)$ of the AMD, AMD+GCM, and RGM. calculations. The calculated densities scaled with a factor $I_f \equiv \sqrt{2J_f + 1}$. are plotted.